Chemical Engineering Journal 156 (2010) 432–445

Contents lists available at ScienceDirect

Chemical Engineering Journal

journal homepage: www.elsevier.com/locate/cej

CFD simulations of segregating fluidized bidisperse mixtures of particles differing in size

Luca Mazzei[a,*], Agostino Casillo[b], Paola Lettieri[a], Piero Salatino[b]

[a] Department of Chemical Engineering, University College London, Torrington Place, London WC1E 7JE, UK
[b] Dipartimento di Ingegneria Chimica, Università degli Studi di Napoli Federico II, P.le Tecchio, 80125 Napoli, Italy

ARTICLE INFO

Article history:
Received 8 July 2009
Received in revised form 21 October 2009
Accepted 4 November 2009

Multiphase flows
Fluidization
Segregation
Mixing
CFD

ABSTRACT

In this work, we use a multifluid model to investigate numerically the dynamics of segregating fluidized bidisperse mixtures. The model uses the default multifluid equations of commercial computational fluid dynamics (CFD) codes, except for the fluid–particle drag force closure, which Mazzei and Lettieri [1] recently developed and extended to polydisperse systems. The study also comprises some preliminary simulations of collapsing monodisperse beds, focusing on the role of the plastic solid stress. This work tests whether the model is able to correctly predict not only the axial segregation profiles through the bed, but also the minimum fluid velocities at which a) the mixture, being no longer fixed, starts segregating and transient fluidization takes place, and b) the mixture becomes steadily fluidized and fully mixed. To validate the model predictions, we use the experimental findings of Marzocchella et al. [2]. The plastic stress results to play an important role, rendering the simulations more stable and allowing for larger time steps. The model well predicts the stationary axial segregation profiles, and for short computational times estimates correctly the onset of transient fluidization; for longer computational times, however, the system evolves towards a new steady state where, even if the powder is at maximum packing, it partly segregates. The model overestimates the velocity required to fully mix the suspension, probably because the simulated bubbling is not as vigorous as it is experimentally.

1. Introduction

Many industrial processes taking place in fluidized beds involve polydisperse suspensions of particles that differ in size and/or density; we mention, for instance, catalytic polymerization and cracking, crystallization, sedimentation and classification. When fluidized, these suspensions tend to segregate, because over a broad range of superficial velocities, some particles are only partly supported by the fluid and migrate towards the bottom of the bed. Whether or not segregation is beneficial depends on the application at hand; in classifiers for example is key, whereas in processes that require intimate particle mixing is detrimental. In either case, to properly design and run fluidized beds, engineers need to predict the dynamics of polydisperse mixtures and anticipate how these respond to changes in operating conditions.

Researchers have extensively investigated how dissimilar fluidized particles mix and segregate. Rowe and Nienow [3] reported that in gas-fluidized suspensions the passage of bubbles is the chief mechanism responsible for mixing and segregation. The wakes of the bubbles generated near the gas distributor plate entrain neighboring particles and drag them upwards through the bed; along the way, the wakes exchange their content with the surrounding dense bed (*wake shedding*). These phenomena promote axial mixing, allowing the particles to migrate towards the surface of the bed. At the same time, as the bubbles ascend, particles from above fall through and around them; furthermore, the smaller and denser particles percolate through the interstices created among the bigger and lighter ones by the bubble motion. These phenomena counter those previously described, promoting axial segregation. Mixing and segregation occur therefore concurrently, and their dynamic equilibrium yields axial profiles of particle concentrations. The particles that tend to accumulate near the bed surface are usually referred to as *flotsam*, whereas those that tend to sink down as *jetsam*.

The experimental studies that appear in the extensive literature on polydisperse fluidized mixtures tried to characterize these systems from different angles. Some proposed to determine the minimum fluid velocity necessary to fully fluidized them [4–7], whereas others concentrated on their dynamics [2,8–11]. Even if these investigations have helped us to understand better how multicomponent suspensions behave, the mechanisms underlying mixing and segregation still remain unclear. Gibilaro and Rowe [12] tried to characterize them, developing a mechanistic model that could predict the stationary axial profiles of jetsam concentration

---

* Corresponding author. Tel.: +44 020 7679 7868; fax: +44 020 7383 2348.
E-mail address: l.mazzei@ucl.ac.uk (L. Mazzei).

1385-8947/$ – see front matter © 2009 Elsevier B.V. All rights reserved.
doi:10.1016/j.cej.2009.11.003

Nomenclature

C_D	particle drag force coefficient
C_D^*	particle drag force coefficient
$\mathbf{D}_e$	rate of deformation tensor of fluid (1/s)
$\mathbf{D}_i$	rate of deformation tensor of i th particle phase (1/s)
d_i	particle diameter in i th particle phase (m)
d_{ik}	constitutive function (m)
e_{ik}	coefficient of restitution for collisions between particles of i th and k th phases
$\mathbf{f}_i$	force exerted by fluid on i th particle phase (per unit particle) (kg m/s^2)
$\mathbf{f}_i^d$	drag force exerted by fluid on i th particle phase (per unit particle) (kg m/s^2)
$\mathbf{f}_i^s$	buoyancy force exerted by fluid on i th particle phase (per unit particle) (kg m/s^2)
$\mathbf{f}_{ik}$	force exerted by k th particle phase on i th particle phase (per unit particle) (kg m/s^2)
F_{ik}	friction coefficient
$\mathbf{g}$	gravitational acceleration (m/s^2)
g_i	radial distribution function in i th particle phase
g_{ik}	constitutive function
G_i^d	pseudointernal energy source term in i th particle phase (kg/m s^3)
$\mathbf{I}$	identity tensor
n	Richardson & Zaki exponent
n_i	number density of i th particle phase (1/m^3)
p^*	dimensional constant (kg/m s^2)
p_e	pressure of fluid (kg/m s^2)
p_i	pressure of i th particle phase (kg/m s^2)
p_i^p	plastic pressure of i th particle phase (kg/m s^2)
p_i^v	viscous pressure of i th particle phase (kg/m s^2)
$\mathbf{q}_i$	pseudothermal heat flux in i th particle phase (kg/s^3)
Re_i	particle Reynolds number for i th particle phase
Re_i^*	particle Reynolds number for i th particle phase
$\mathbf{S}_e$	effective stress tensor of fluid (kg/m s^2)
$\mathbf{S}_i$	effective stress tensor of i th particle phase (kg/m s^2)
S_i^c	pseudointernal energy sink term in i th particle phase (kg/m s^3)
S_i^v	pseudointernal energy sink term in i th particle phase (kg/m s^3)
t	time (s)
u	superficial fluid velocity magnitude (m/s)
u_1	minimum superficial velocity at which particle mixture fully fluidizes (m/s)
u_2	minimum superficial velocity at which transient fluidization begins (m/s)
$\mathbf{u}_e$	velocity of fluid (m/s)
$\mathbf{u}_i$	velocity of i th particle phase (m/s)
U_i	pseudointernal energy of i th particle phase (m^2/s^2)
x	axial coordinate (m)

Greek symbols

β_i	drag force (between fluid and i th particle phase) coefficient (kg/m^3 s)
ε	volume fraction of fluid
ε_{min}	volume fraction of fluid at maximum packing
κ_e	dilatational viscosity of fluid (kg/m s)
κ_i	dilatational viscosity of i th particle phase (kg/m s)
κ_i^v	dilatational viscosity of i th particle phase in viscous regime (kg/m s)
μ_e	shear viscosity of fluid (kg/m s)
μ_i	shear viscosity of i th particle phase (kg/m s)
μ_i^p	shear viscosity of i th particle phase in plastic regime (kg/m s)
μ_i^v	shear viscosity of i th particle phase in viscous regime (kg/m s)
Θ_i	granular temperature of i th particle phase (m^2/s^2)
ρ_e	mass density of fluid (kg/m^3)
ρ_i	mass density of i th particle phase (kg/m^3)
ϕ_f	frictional solid packing
ϕ_i	volume fraction of i th particle phase
ϕ_{max}	maximum solid packing
ϕ_m^i	volume fraction of i th particle phase at maximum solid packing
φ	constitutive function
ω_i	mass fraction i th particle phase on fluid-free basis
ξ_{ik}	constitutive function
ψ	constitutive function
ζ_{ik}	drag force (between i th and k th particle phases) coefficient (kg/m^3 s)

in bidisperse fluidized beds. Since then, several researchers have made similar attempts, improving on Gibilaro and Rowe's model or advancing alternative approaches [13–16]. Their equations reproduce reasonably well the main qualitative features of powder segregation, although there are some exceptions [10], but they are quantitatively inaccurate and rely on (perhaps too) many empirical parameters.

The increased power of desktop computers permits today to simulate the dynamics of multicomponent mixtures by integrating numerically their equations of motion. Being based on first principles (conservation of mass, momentum and energy), these equations should describe quite accurately the dynamics of granular media. In reality, nevertheless, this is more a promise than a fact. Two modeling approaches are available: the Eulerian multifluid, where averaged equations describe the motion of both fluid and particles, regarded as interpenetrating continua, and the Eulerian–Lagrangian, which tracks each particle and solves averaged equations of motion only for the continuous phase. Although the first approach is convenient because it is relatively inexpensive numerically and provides directly the information that usually interests us (*e.g.*, mean pressure drops, average velocity fields, void fraction profiles), the other is also frequently used, especially by academics, insomuch as it offers considerable insight, at a more fundamental level, into the dynamics of granular media [17–20].

Multifluid models originate from the work of [21], who were the first to derive averaged equations of motion for monodisperse fluidized suspensions. Adopting various averaging schemes, researchers have formulated many variants to the original equations, extending them also to polydisperse mixtures [22]. These equations share one feature: they comprise indeterminate terms not directly related to the averaged variables but still associated with details of the motion at a length scale much smaller than the mean particle size. These terms are represented by the fluid and solid effective stress tensors and by the interaction forces exchanged by the phases. Thus, a closure problem arises, which usually cannot be solved analytically and needs to be overcome by means of semiempirical expressions. This is the main shortcoming of the method, for finding good closures is exceedingly difficult, but inaccurate closures lead to poor model predictions.

For the fluid–particle interaction force there are many expressions derived from empirical pressure drop or equilibrium bed expansion profiles in homogeneous suspensions [22]. Modeling particle interactions is much more difficult; to do it, researchers often resort to the kinetic theory of dense granular flows. Initially developed for monodisperse mixtures to close the effective solid stress tensor [23–25], these kinetic equations have then been extended to multicomponent systems to express not only the stress but also the particle interactions between the granular phases [26–29]. The averaged equations of motion, coupled with these constitutive expressions, have permitted to simulate the dynamics of polydisperse granular media. Nonetheless, albeit these models describe correctly their qualitative features, predicting for instance axial segregation [30], layer inversion [31] and the entrainment of particles in the bubble wakes [32], they still fail to predict important basic fluidization parameters, such as the minimum superficial fluid velocity at which a bidisperse mixture starts segregating or becomes fully mixed and steadily fluidized.

2. Fluidized bidisperse mixture dynamics. Experimental evidence

As we mentioned, many researchers have investigated experimentally the dynamics of polydisperse fluidized mixtures. For a thorough analysis, very clearly presented, we refer to the work of [2] and [10], whose results we now only in part briefly summarize.

Let us consider a bidisperse powder of particles with equal density and different diameter. Initially the powder is perfectly mixed, with a jetsam volume fraction on a fluid-free basis (that is, not accounting for the interparticle voidage) equal to ω_1. For low superficial fluid velocities, the powder remains fixed and the pressure drop $\Delta p(u)$ through it increases linearly. When u reaches the value $u_1(\omega_1)$, Δp equals the weight of the bed per unit cross-sectional area: it seems therefore that the powder has become fluidized. For higher superficial fluid velocities, nevertheless, $\Delta p(u)$ does not remain constant, as we would expect, but oscillates giving rise to a sawlike pattern, a behavior that reveals transient fluidization. The powder is no longer fully supported by the fluid, but the jetsam segregates forming a defluidized layer of particles that partly rests on the distributor plate, lowering the pressure drop. Hence, the bed splits up in two regions: one fully fluidized and one defluidized. When u reaches the value $u_2(\omega_1)$, Δp equals once again the weight of the bed per unit cross-sectional area, and remains constant at higher superficial fluid velocities. Thus, $u_2(\omega_1)$ represents the minimum velocity necessary to fully and steadily fluidize all the particle mixture, whereas $u_1(\omega_1)$ represents the minimum velocity at which the bed is no longer fixed, the particles start moving, transient fluidization takes place and $\Delta p(u)$ begins oscillating. These velocities depend on ω_1, but are not related to the minimum fluidization velocities of flotsam and jetsam; in fact, $u_1(\omega_1)$ might be lower than the former, whereas $u_2(\omega_1)$ is always lower than the latter. Note that when u exceeds $u_1(\omega_1)$, the bed starts bubbling, allowing the jetsam to segregate. In the range $[u_1(\omega_1), u_2(\omega_1)]$, the fluid does not support the jetsam, which sinks down forming a *partially* defluidized layer; we emphasize the word partially, because experimental evidence shows that the layer is near incipient fluidization, being supported *almost entirely* by the fluid. When u exceeds $u_2(\omega_1)$, all the particles float freely, mixing is vigorous and overtakes segregation, and the mixture is perfectly mixed. No segregation, therefore, occurs for u greater than $u_2(\omega_1)$.

3. Goals of this work

This work tests a basic multifluid model implemented within the commercial computational fluid dynamics (CFD) code Fluent, verifying whether it yields the correct segregation profiles and fluidization parameters for bidisperse mixtures of particles differing only in size. In light of the experimental findings described in the previous section, we aim to answer, among others, the following questions:

Table 1
Material properties.

Property	Units	Silica Sand (Flotsam)	Glass Beads (Jetsam)
Sauter mean diameter	μm	125	500
Size	μm	100–150	400–600
Sphericity	–	≈ 1	1
Density	kg/m^3	2600	2540
Geldart group	–	B	B
Terminal velocity	m/s	0.80	4.10
Minimum fluidization velocity	m/s	0.017	0.220

(1) For a given powder, initially perfectly mixed and with a jetsam concentration on a fluid-free basis equal to $\bar{\omega}_1$, is the model able to correctly predict $u_1(\bar{\omega}_1)$ and $u_2(\bar{\omega}_1)$? In particular, is $u_2(\bar{\omega}_1)$ less than the jetsam minimum fluidization velocity?
(2) For u in the range $[u_1(\bar{\omega}_1), u_2(\bar{\omega}_1)]$, does the bed separate in two layers, one fluidized and one defluidized but near incipient fluidization?
(3) Are the axial profiles of jetsam volume fraction correctly predicted in the two layers? Is each layer well mixed, or does $\omega_1(x)$ change gradually along the axial coordinate x?

Some researchers have simulated bidisperse fluidized suspensions, aiming to predict their axial segregation profiles (see, for instance [30]). These studies, however, do not attempt to predict the threshold velocities $u_1(\bar{\omega}_1)$ and $u_2(\bar{\omega}_1)$. We believe that this is an important test for a multiphase fluid dynamic model. If a model is accurate, it must be able to describe the phenomenology presented above, and predict correctly the values of these two simple, but crucial, fluidization parameters.

4. Materials

To answer the questions raised in Section 3 and validate the model, we must compare numerical predictions with experimental data. To this end, we did not run experiments ourselves, but used the results of [2]. Table 1 shows the material properties. The bed consists of a binary mixture containing equal masses ($\bar{\omega}_1 = 0.50$) of 125 μm silica sand particles (flotsam) and 500 μm glass beads (jetsam). The ratio between their minimum fluidization velocities is about 13.

5. Multiphase fluid dynamic model

We employ a multifluid modeling approach. The averaged equations of motion are six, two for each phase, and express the principle of conservation of mass (continuity equations) and linear momentum (dynamical equations). These do not form a closed system, and require closure relationships.

Table 2 reports the averaged equations of motion [22,33]. i is a phase index, with 1 and 2 identifying jetsam and flotsam,

Table 2
Multifluid locally averaged equations of motion for a system of two particle classes.

Continuity Equation—Fluid Phase

$$\frac{\partial \varepsilon}{\partial t} + \nabla \cdot (\varepsilon u_e) = 0$$

Continuity Equation—Solid Phase i

$$\frac{\partial \phi_i}{\partial t} + \nabla \cdot (\phi_i u_i) = 0$$

Dynamical Equation—Fluid Phase

$$\rho_e \left[\frac{\partial}{\partial t}(\varepsilon u_e) + \nabla \cdot (\varepsilon u_e u_e) \right] = \nabla \cdot S_e - n_1 f_1 - n_2 f_2 + \varepsilon \rho_e g$$

Dynamical Equation—Solid Phase i

$$\rho_i \left[\frac{\partial}{\partial t}(\phi_i u_i) + \nabla \cdot (\phi_i u_i u_i) \right] = \nabla \cdot S_i + n_i f_i + n_i f_{ik} + \phi_i \rho_i g$$

respectively. ρ_e and ρ_i are the densities of the fluid and of the particles, respectively; ε and ϕ_i are their volume fractions; n_i is the number density of solid phase i, and $\mathbf{g}$ is the gravitational acceleration. Furthermore, $\mathbf{u}_e$, $\mathbf{u}_i$, $\mathbf{S}_e$, $\mathbf{S}_i$, $\mathbf{f}_i$ and $\mathbf{f}_{ik}$ are the averaged velocities, effective stress tensors and interaction forces per unit particle exerted by the fluid and by the k th solid phase on the i th solid phase, respectively.

5.1. Fluid–particle interaction forces

The fluid–particle interaction force consists of buoyancy and drag forces. Some other contributions should be considered, for instance, the virtual mass, lift and Faxen forces, and a history-dependent term analogous to the Basset force for the motion of isolated particles [34]. These additional contributions are neglected; we thoroughly discussed the reasons in [35] and do not repeat them here. Thus, we write $\mathbf{f}_i = \mathbf{f}_i^s + \mathbf{f}_i^d$, defining the buoyancy force as $n_i \mathbf{f}_i^s \equiv -\phi_i \nabla p_e$ and closing the drag force using the expression of [1]:

$$n_i \mathbf{f}_i^d \equiv \beta_i(\mathbf{u}_e - \mathbf{u}_i) \quad ; \quad \beta_i = \frac{3}{4} C_D(Re_i) \frac{\rho_e \|\mathbf{u}_e - \mathbf{u}_i\| \varepsilon \phi_i}{d_i} \varepsilon^{-\psi(\varepsilon, Re_i)} \tag{5.1}$$

where it is:

$$\begin{aligned} &\psi(\varepsilon, Re_i) \equiv -\frac{\ln \varphi(\varepsilon, Re_i)}{\ln \varepsilon} \quad ; \quad \varphi(\varepsilon, Re_i) \equiv \frac{C_D^*(\varepsilon, Re_i)}{C_D(Re_i)} \; \varepsilon^{2(1-n)} \\ &C_D(Re_i) = \left(0.63 + 4.8 Re_i^{-1/2}\right)^2 \; ; \; C_D^*(Re_i^*) = \left(0.63 + 4.8 Re_i^{*\,-1/2}\right)^2 \\ &Re_i \equiv \frac{\rho_e}{\mu_e} \varepsilon \|\mathbf{u}_e - \mathbf{u}_i\| d_i \quad ; \quad Re_i^*(\varepsilon, Re_i) \equiv \frac{Re_i}{\varepsilon^n} \quad ; \\ &n(Re_i^*) = \frac{4.8 + 2.4 \cdot 0.175 Re_i^{*3/4}}{1 + 0.175 Re_i^{*3/4}} \end{aligned} \tag{5.2}$$

Here d_i is the particle diameter of the i th solid phase, Re_i and Re_i^* are particle Reynolds numbers, C_D and C_D^* are drag coefficients evaluated with the relation of [36] and n is the [37] coefficient evaluated with the equation of [38].

5.2. Particle–particle interaction forces

We assume that the interaction force $\mathbf{f}_{ik}$ exchanged between particles of different phases includes only a drag-like contribution, being thus proportional to the slip velocity between the phases. To close it, we adopt the constitutive equation of [27]:

$$\begin{aligned} &n_i \mathbf{f}_{ik} \equiv \zeta_{ik}(\mathbf{u}_k - \mathbf{u}_i) \quad ; \\ &\quad \zeta_{ik} = \frac{3}{4}(1 + e_{ik}) \left(1 + \frac{\pi}{4} F_{ik}\right) \frac{\rho_i \rho_k \phi_i \phi_k g_{ik} (d_i + d_k)^2}{\rho_i d_i^3 + \rho_k d_k^3} \|\mathbf{u}_k - \mathbf{u}_i\| \end{aligned} \tag{5.3}$$

where e_{ik} is a coefficient of restitution equal to 0.90, F_{ik} is a coefficient of friction equal to 0.15 and g_{ik} represents a radial distribution function that we obtain by combining the radial distribution functions g_i and g_k of the i th and k th particle phases, respectively. Their expressions are:

$$g_i = \frac{d_i}{2} \sum_{k=1}^{2} \frac{\phi_k}{d_k} + \left[1 - \left(\frac{\phi}{\phi_{max}}\right)^{1/3}\right]^{-1} \quad ; \quad g_{ik} = \frac{d_i g_k + d_k g_i}{d_i + d_k} \tag{5.4}$$

Here ϕ is the overall solid volume fraction, and ϕ_{max} is the maximum solid compaction, *i.e.*, the maximum value that ϕ can attain. The latter is a function of the powder composition, which we determine by using the empirical expression of [39]:

$$\begin{aligned} &\phi_{max} = \phi_m^i + (1 - \xi_{ik}) \left[\phi_m^i + (1 - \phi_m^i)\phi_m^k\right] (1 - \omega_i) \\ &\qquad \text{for} \quad \omega_i \geq \frac{\phi_m^i}{\phi_m^i + (1 - \phi_m^i)\phi_m^k} \end{aligned} \tag{5.5}$$

or otherwise:

$$\begin{aligned} &\phi_{max} = \phi_m^k + \left[(\phi_m^i - \phi_m^k) + (1 - \xi_{ik})(1 - \phi_m^i)\phi_m^k\right] \\ &\qquad \left[\phi_m^i + (1 - \phi_m^i)\phi_m^k\right] \frac{\omega_i}{\phi_m^i} \end{aligned} \tag{5.6}$$

In the relations above, ϕ_m^i and ϕ_m^k are the particle volume fractions at maximum packing for the phases i and k, respectively; also, it is:

$$\omega_i = \frac{\phi_i}{\phi} \quad ; \quad \xi_{ik} \equiv \left(\frac{d_k}{d_i}\right)^{1/2} \quad \text{with} \quad d_i \geq d_k \tag{5.7}$$

The relations above hold for d_i greater than d_k; as a consequence, phases i and k must represent jetsam and flotsam, respectively. Note that, whereas Eq. (5.4) holds for any polydisperse mixtures (if we replace the summation limit with n), Fedors and Landel's model applies only to bidisperse mixtures.

5.3. Effective stress

We close the effective stress tensors using customary Newtonian constitutive equations [40]; accordingly, we write:

$$\begin{aligned} &\mathbf{S}_e = -p_e \mathbf{I} + 2\mu_e \mathbf{D}_e + \left(\kappa_e - \frac{2}{3}\mu_e\right) \operatorname{tr}\mathbf{D}_e \mathbf{I} \quad ; \\ &\qquad \mathbf{S}_i = -p_i \mathbf{I} + 2\mu_i \mathbf{D}_i + \left(\kappa_i - \frac{2}{3}\mu_i\right) \operatorname{tr}\mathbf{D}_i \mathbf{I} \end{aligned} \tag{5.8}$$

where p_e, p_i, μ_e, μ_i, κ_e and κ_i are the averaged pressures, shear viscosities and dilatational viscosities of the fluid and particle phases, respectively; moreover, $\mathbf{I}$ is the identity tensor, while $\mathbf{D}_e$ and $\mathbf{D}_i$ are the rate of deformation (or strain) tensors, which are defined as:

$$\mathbf{D}_e \equiv \frac{1}{2}\left(\nabla \mathbf{u}_e + \nabla \mathbf{u}_e^T\right) \quad ; \quad \mathbf{D}_i \equiv \frac{1}{2}\left(\nabla \mathbf{u}_i + \nabla \mathbf{u}_i^T\right) \tag{5.9}$$

Closing $\mathbf{S}_e$ and $\mathbf{S}_i$ therefore reduces to finding constitutive expressions for the pressure, shear viscosity and dilatational viscosity of each phase. We regard the fluid as incompressible, and do not specify its pressure constitutively; furthermore, we assume that μ_e is constant, and neglect κ_e. For the solid phases, conversely, we adopt more elaborate closures.

Two parameters characterize a polydisperse powder: the maximum solid packing ϕ_{max} and the frictional solid packing ϕ_f. The first is a geometrical property of the particles and, as previously said, indicates the maximum volume fraction that the solid can reach; the second marks the transition from the viscous to the plastic flow regime. In the first regime, the particles undergo transient contacts, momentum transfer is translational and collisional, and the granular kinetic theory holds; in the second, the particles undergo enduring contacts, momentum transfer is mainly frictional and other models, empirical, phenomenological or based on soil mechanics theory, apply.

In both regimes, each granular phase is usually modeled as a Newtonian continuum, characterized in the viscous flow regime by a viscous solid pressure p_i^v, a viscous shear viscosity μ_i^v and a viscous dilatational viscosity κ_i^v, and in the plastic flow regime by a plastic solid pressure p_i^p, a plastic shear viscosity μ_i^p and a plastic dilatational viscosity κ_i^p. In the viscous regime, the generic property f_i coincides with f_i^v, whereas in the plastic regime it is assumed to be equal to $f_i^v + f_i^p$.

In this work, we express p_i^v using the closure of [41], suitably extended to cater for polydisperse suspensions [25]:

$$p_i^v = \left[1 + 2\sum_{k=1}^{2}\left(\frac{d_{ik}}{d_i}\right)^3 (1+e_{ik})\phi_k g_{ik}\right]\phi_i\rho_i\Theta_i \qquad \text{where} \quad d_{ik} \equiv \frac{d_i+d_k}{2} \tag{5.10}$$

Here Θ_i is the granular temperature of the i th phase, related to the kinetic energy of the fluctuating particle motion. For $k = i$, e_{ii} coincides with the restitution coefficient e_i, whereas, from Eq. (5.4), g_{ii} reduces to g_i. For the viscous shear viscosity, we adopt the closure of [25]:

$$\mu_i^v = \frac{10\rho_i d_i\sqrt{\pi\Theta_i}}{96(1+e_i)g_i}\left[1+\frac{4}{5}(1+e_i)\phi_i g_i\right]^2 + \frac{4}{5}\phi_i^2\rho_i d_i g_i(1+e_i)\left(\frac{\Theta_i}{\pi}\right)^{1/2} \tag{5.11}$$

and for the viscous dilatational viscosity that of [41]:

$$\kappa_i^v = \frac{4}{3}\phi_i^2\rho_i d_i g_i(1+e_i)\left(\frac{\Theta_i}{\pi}\right)^{1/2} \tag{5.12}$$

These expressions are those originally developed for monodisperse suspensions and do not directly account for the presence of the other granular phases.

The granular temperatures are governed by balance equations for pseudointernal energies related to the particle velocity fluctuations [25,42]. For fluidized mixtures these equations differ from the classical internal energy balance equation because of a sink term S_i^c representing losses of pseudointernal energy caused by inelastic collisions, a source term G_i^d representing the generation of particle velocity fluctuations by fluctuating fluid–particle forces, and a sink term S_i^v representing their dampening by the viscous resistance to particle motion. Accordingly, each balance equation reads:

$$\rho_i\left[\frac{\partial}{\partial t}(\phi_i U_i)+\nabla\cdot(\phi_i U_i\mathbf{u}_i)\right] = -\nabla\cdot\mathbf{q}_i + \mathbf{S}_i : \nabla\mathbf{u}_i + G_i^d - S_i^v - S_i^c \tag{5.13}$$

where $U_i \equiv 3\Theta_i/2$ is the pseudointernal energy per particle unit mass and $\mathbf{q}_i$ is the pseudothermal heat flux. The closure problem then requires finding constitutive expressions also for $\mathbf{q}_i$, S_i^v, S_i^c and G_i^d. We do not report them here for briefness, but refer to [25].

The plastic granular stress is often modeled with arbitrary functions, which have no theoretical basis but correctly describe *qualitatively* how dense granular media behave [42]. The prime feature that must be captured is that such materials cannot reach compactions that are unphysically high. A closure for the plastic solid pressure that many modelers employ takes the form:

$$p_i^p = \phi_i p^* \quad \text{where} \quad p^* \equiv 10^A(\phi-\phi_f)^B \tag{5.14}$$

where the coefficients A and B are very high, with typical values of 25 and 10, respectively. This equation is extremely sensitive to the deviation of ϕ from ϕ_f and this may lead to big pressure fluctuations and violent numerical instabilities that could crash the simulation [43,44]. For this reason, we decided not to use it.

Eq. (5.14) is often employed with radial distribution functions that are bounded and do not diverge positively when ϕ approaches ϕ_{max}. For instance, the model of [42], implemented in the numerical code MFIX, adopts the following expression:

$$g_i = \frac{1}{\varepsilon}\left(1 + \frac{3d_i}{2\varepsilon}\sum_{k=1}^{2}\frac{\phi_k}{d_k}\right) \tag{5.15}$$

in which, as opposed to Eq. (5.4), ϕ_{max} does not feature. Since the closure that we selected for g_i does diverge when ϕ approaches ϕ_{max}, the viscous solid pressure already prevents the mixture from overpacking, and therefore there is no need to replace Eq. (5.10) with any arbitrary divergent function, qualitatively sound but theoretically unfounded.

These considerations induced us to adopt the so-called KTGF-based model, a plastic model partly based on the kinetic theory of granular flows. This accounts only for the plastic shear viscosity μ_i^p, neglecting the plastic solid pressure p_i^p and the plastic dilatational viscosity κ_i^p. When ϕ exceeds ϕ_f, we keep on using the viscous closure for the solid pressure, Eq. (5.10), but we increase the shear solid viscosity by adding to the viscous contribution, Eq. (5.11), a frictional one, whose expression is [43]:

$$\mu_i^p = \frac{p_i\sin\vartheta_i}{2\sqrt{I_2(\mathbf{D}_i)}} = \frac{p_i^v\sin\vartheta_i}{2\sqrt{I_2(\mathbf{D}_i)}} \quad ; \quad I_2(\mathbf{D}_i) \equiv \frac{1}{2}\left[(\mathrm{tr}\mathbf{D}_i)^2 - \mathrm{tr}\mathbf{D}_i^2\right] \tag{5.16}$$

where ϑ is the angle of internal friction of the i th granular material, and $I_2(\mathbf{D}_i)$ is the second invariant of the rate of deformation tensor $\mathbf{D}_i$. In the pseudointernal energy balance equation, the higher viscosity generates a higher dissipation of mechanical energy into pseudointernal energy, increasing the granular temperature and in turn the viscous solid pressure; therefore, the plastic shear viscosity indirectly affects the solid pressure, despite our setting p_i^p to zero. As we shall see in Section (8), by slowing down the solid packing, this mechanism increases numerical stability and allows us to use bigger time steps compared with simulations where we neglect the plastic stress entirely.

6. Boundary and initial conditions

The computational grid (uniform, with square cells of 5 mm side) is two-dimensional; hence, front and back wall effects are neglected. On the left and right walls, no-slip boundary conditions apply. At the bottom of the bed, a uniform inlet fluid velocity u is specified. The fluid is ambient air. At the domain upper boundary, the pressure is set to 10^5 Pa. On all the boundaries, the solid mass fluxes are set to zero.

In its initial state, the bed is fixed and made up of a perfectly mixed powder with jetsam volume fraction on a fluid-free basis equal to 0.50. The bed is 0.40 m high, whereas the vessel is 1.00 m high. The voidage is everywhere set to 0.40; this is just a reference value, and does not coincide with the minimum voidage $\varepsilon_{min} = 1 - \phi_{max}$ predicted by the model of [39]. Accordingly, depending on how we operate the bed, the voidage might decrease.

7. Numerical schemes and techniques

To run the simulations, we employed the commercial CFD code Fluent 6.3. The governing and constitutive equations were implemented in the multifluid model of the package, which is based on a Eulerian description of the flow. We used the pressure-based solver, which is recommended for low-speed incompressible flows. To convert scalar transport equations into algebraic equations that can be solved numerically, the code adopts a finite-volume discretization scheme. To ensure convergence, we discretized in space through a first-order upwind scheme, where cell-face quantities are determined by assuming that the cell-center values of any field variable represent cell-averages that hold throughout the entire cells; thus, face quantities are identical to cell quantities, and are set equal to the cell-center values in the upstream cells (relative to the direction of the normal velocity). Temporal discretization is first order accurate and implicit. To couple pressure and velocity, we adopted the SIMPLE (Simultaneous Solu-

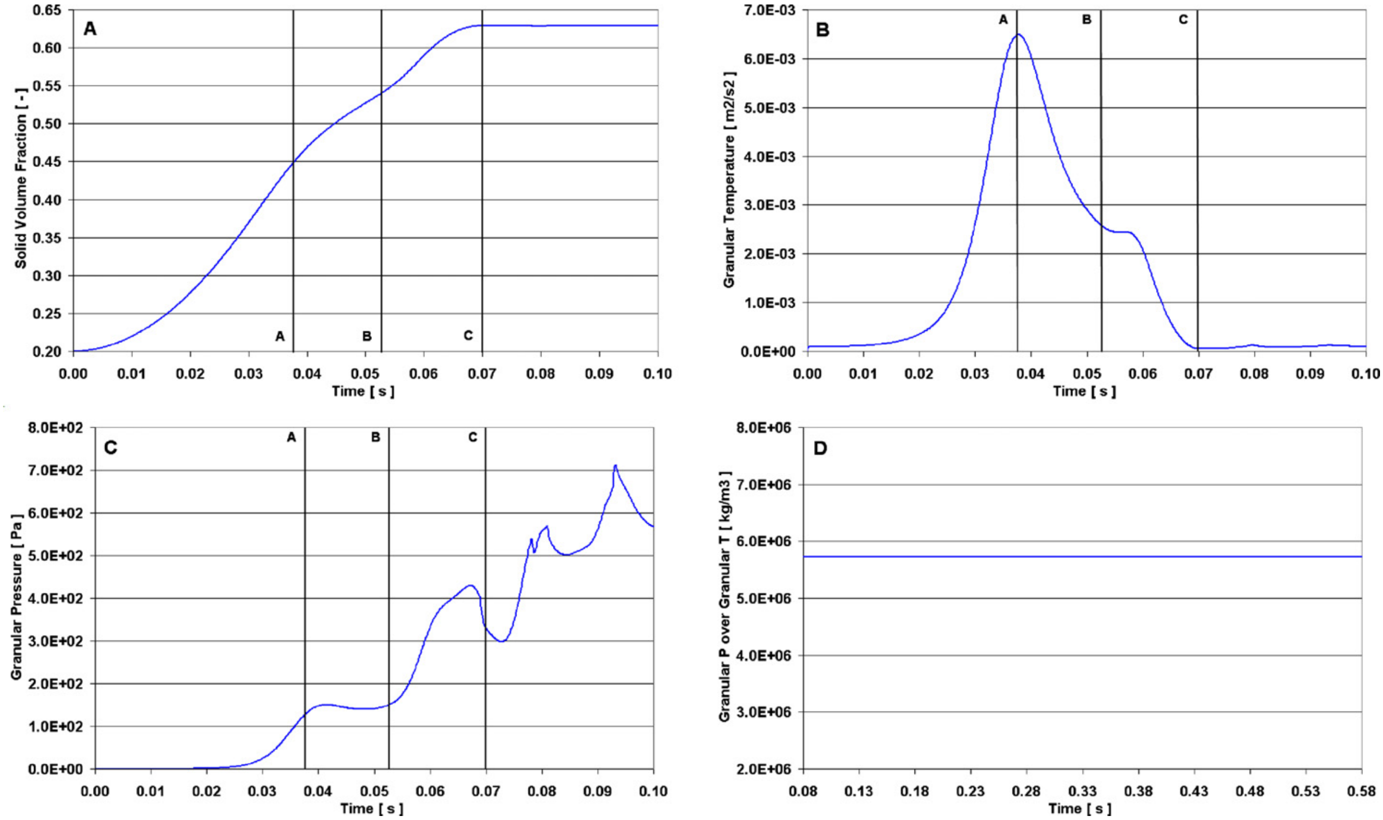

Fig. 1. Solid volume fraction, granular temperature and granular pressure time profiles in the reference location of the bed during the bed collapse. The plastic solid stress is neglected. The time step is equal to 10^{-4} s.

tion of Non-linearly Coupled Equations) algorithm of [45]; the code does not allow any other coupling algorithms for Eulerian multiphase calculations. At each time step, we used a maximum of 200 iterations to compute the flow variables. Setting the tolerance to 10^{-5}, we usually attained convergence within the iteration limit. The time step was set to 10^{-3} s (see Section (8)). Under-relaxation factors of 0.20 were adopted for all the variables.

8. Preliminary simulations. Plastic stress role and time step selection

Before studying segregating fluidized bidisperse powders, we ran some preliminary simulations involving monodisperse collapsing beds. Investigating these simple systems permits, in short computational times, to 1) test the numerical stability of the model when the suspension rapidly overpacks, like in fast segregating beds, 2) understand better how the granular material behaves and how the fluid dynamic variables affect one another, *e.g.*, plastic viscosity and granular temperature, 3) analyze the role played by the plastic solid stress and 4) select the shortest time step that ensures invariance of the numerical results.

A uniform suspension, initially with a solid volume fraction equal to 0.20, freely collapses in a stagnant fluid. Since we do not fluidize the powder, the suspension cannot preserve its expanded state and contracts, its solid volume fraction increasing until it reaches the value ϕ_{max}. Investigating this systems is convenient, for the dynamics are fast and results can be obtained rapidly; moreover, the quickness with which ϕ increases is likely to accent numerical instabilities, if these are present. We ran six simulations, three accounting for the plastic stress and three neglecting it, using time steps of 10^{-2}, 10^{-3} and 10^{-4} s. In each simulation, we monitored the temporal evolution of the fluid dynamic variables of interest in a reference location at the bottom of the bed, near the distributor center, since this is the most critical region of the bed and also the one which reaches stationary conditions first. We considered only the jetsam material, because its particles collapse faster. Since one solid phase is present, we replace the phase index i with the index p, except for ϕ that represents both jetsam and overall solid volume fractions.

8.1. Simulations without plastic stress

In these simulations, we did not account for the plastic stress; consequently, we closed the effective solid stress tensor using only the granular kinetic theory model. From Eq. (5.10), we can express the viscous solid pressure as $p_p^v(\phi, \Theta_p) = f(\phi)\Theta_p$, where $f(\phi)$ is a monotonic increasing function of ϕ whose rate of change rapidly rises as ϕ approaches ϕ_{max}.

Let us first describe the results that we obtained using a time step of 10^{-4} s. Fig. 1 reports the time profiles of jetsam volume fraction, granular temperature and granular pressure in the reference location of the bed; here the steady state is reached within 0.1 real time seconds, which correspond to 1000 simulation time steps. Note that this is not the time that the whole system takes to attain stationary conditions, the latter being about 1.5 real time seconds. Three time intervals are significant, identified in the diagrams by the lines A, B and C; these refer to the real time instants $t_A = 0.038$ s,$t_B = 0.053$ s and $t_C = 0.070$ s, respectively. For $t < t_A$, since both ϕ and Θ_p increase, the granular pressure does the same; note, nevertheless, that Θ_p seems to affect more strongly $p_p^v(\phi, \Theta_p)$. For $t_A \le t < t_B$, ϕ increases whereas Θ_p decreases; these two effects balance themselves out, leaving the granular pressure roughly constant. For $t_B \le t < t_C$, ϕ and Θ_p preserve their trends; initially, since

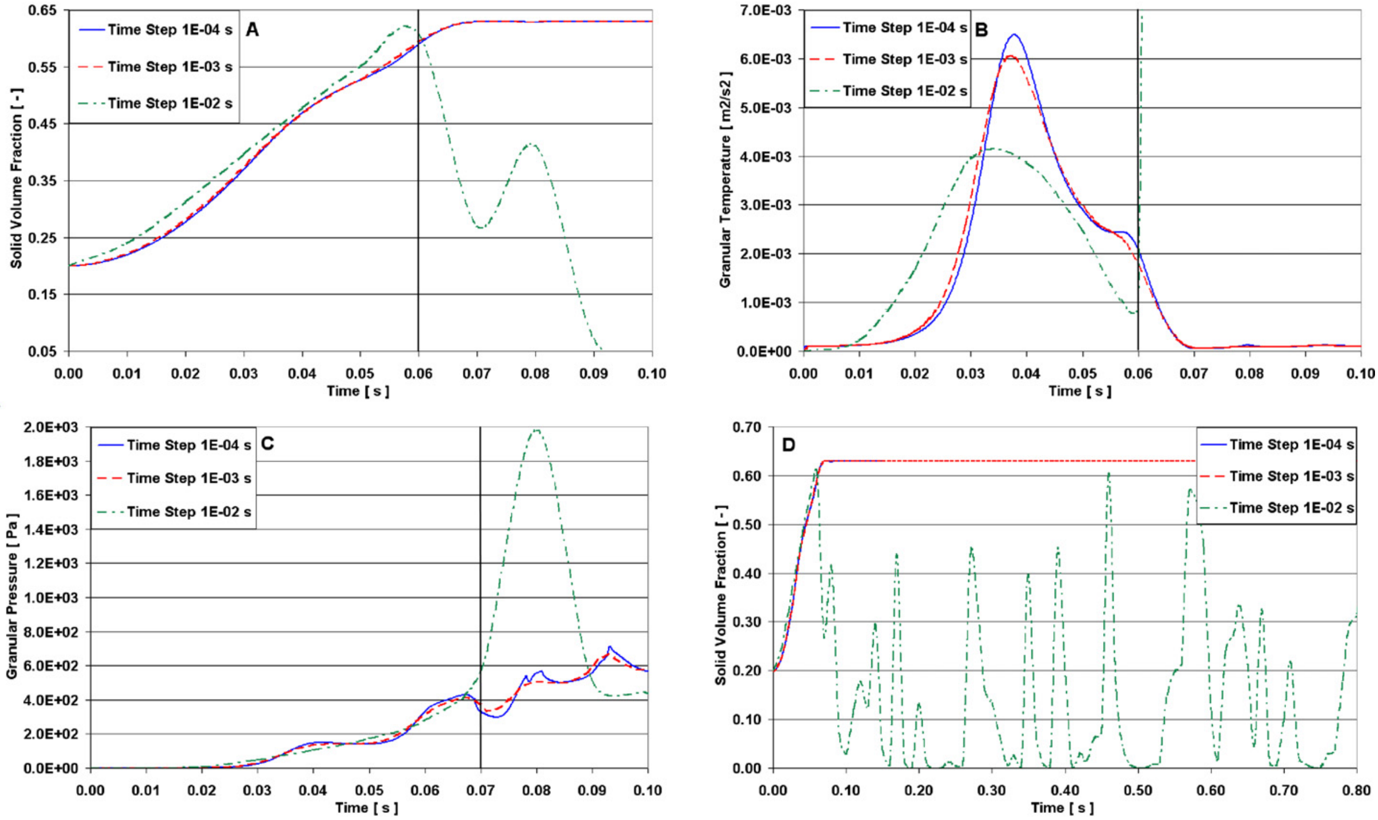

Fig. 2. Solid volume fraction, granular temperature and granular pressure time profiles in the reference location of the bed during the bed collapse. The plastic solid stress is neglected. The time steps are equal to 10^{-4}, 10^{-3} and 10^{-2} s.

Θ_p changes much more slowly than ϕ, the latter dictates the behavior of $p_p^v(\phi, \Theta_p)$, which rises up quickly; afterwards, the situation reverses and $p_p^v(\phi, \Theta_p)$ starts decreasing. For $t \geq t_C$, ϕ no longer changes and $p_p^v(\phi, \Theta_p)$ perfectly mirrors the granular temperature; in particular, the ratio $f(\phi) = p_p^v(\phi, \Theta_p)/\Theta_p$ is constant, as Fig. 1D indicates.

Even if we have used the granular kinetic theory model also in the plastic regime, where it no longer applies, the results are qualitatively correct. This is because the expression for the radial distribution function herein adopted, Eq. (5.10), handles correctly the transition from the compressible to the incompressible granular regimes. Let us now analyze how the time step influences the simulation output. Fig. 2 reports the same profiles shown in Fig. 1 for the three different time steps used. As we can observe, time steps of 10^{-3} and 10^{-4} s yield essentially the same results; a time step of 10^{-2} s instead is too large and generates numerical instabilities. These appear after 0.06 real time seconds and lead to mass imbalance: solid is lost from the reference cell, as if it were destroyed. The solid volume fraction, instead of continuing to increase towards ϕ_{max}, abruptly drops down to unphysically low values; at the same time, the granular temperature overshoots reaching values several orders of magnitude greater than the correct ones ($10^{-1}\,\mathrm{m}^2/\mathrm{s}^2$ instead of $10^{-5}\mathrm{m}^2/\mathrm{s}^2$). This would result in extremely high granular pressures if the solid mass were not lost; in spite of mass imbalance, nevertheless, the pressure reaches unphysically high values anyway. For longer times, the solid volume fraction oscillates periodically, going up when more solid reaches the reference cell from higher regions of the bed and going down again when the solid mass is once again lost; Fig. 2D shows this behavior. This analysis tells us that, if we neglect the plastic stress, the optimal time step is 10^{-3} s; with smaller time steps the results do not vary appreciably.

8.2. Simulations with plastic stress

Again, we first present the results obtained using a time step of 10^{-4} s. Fig. 3 reports the time profiles of jetsam volume fraction, granular temperature and granular pressure in the reference location of the bed. In this case, four time intervals are significant, identified in the diagrams by the lines A, B, C and D; these refer to the real time instants $t_A = 0.038\mathrm{s}$,$t_B = 0.053\mathrm{s}$,$t_C = 0.061\mathrm{s}$ and $t_D = 0.080\mathrm{s}$, respectively. Between t_A and t_C the system behaves as before. Initially, ϕ and Θ_p both increase, and the granular pressure follows suit; then the pressure temporarily stabilizes, insomuch as ϕ and Θ_p take opposite trends that balance themselves out; successively, Θ_p temporarily plateaus and the pressure rises up again. When ϕ reaches the frictional threshold ϕ_f, the solid viscosity abruptly increases, because the plastic contribution is added to the viscous one. This accelerates the dissipation of mechanical energy into pseudointernal energy. As a consequence, the granular temperature and in turn the granular pressure suddenly rise up; Fig. 3B and C show these abrupt variations, reflected by spikes in the time profiles immediately after t_C. Between t_C and t_D both ϕ and Θ_p affect the granular pressure, and since their trends are opposite, the pressure does not vary monotonically. After t_D, since ϕ has reached its stationary value, $p_p(\phi, \Theta_p)$ perfectly mirrors Θ_p, and once again their ratio is constant, as Fig. 3D indicates.

If we compare the real time instants t_A, t_B and t_D with the corresponding times reported in Section (8.1), we see that the first two coincide, because for $\phi < \phi_f$ the simulations are identical. Conversely, the time that ϕ takes to reach stationary conditions is longer when we account for the plastic stress (0.080 s instead of 0.070 s). We expected this, because when the plastic stress is added to the viscous one, the granular pressure increases and slows down solid compaction. The difference between the two times is

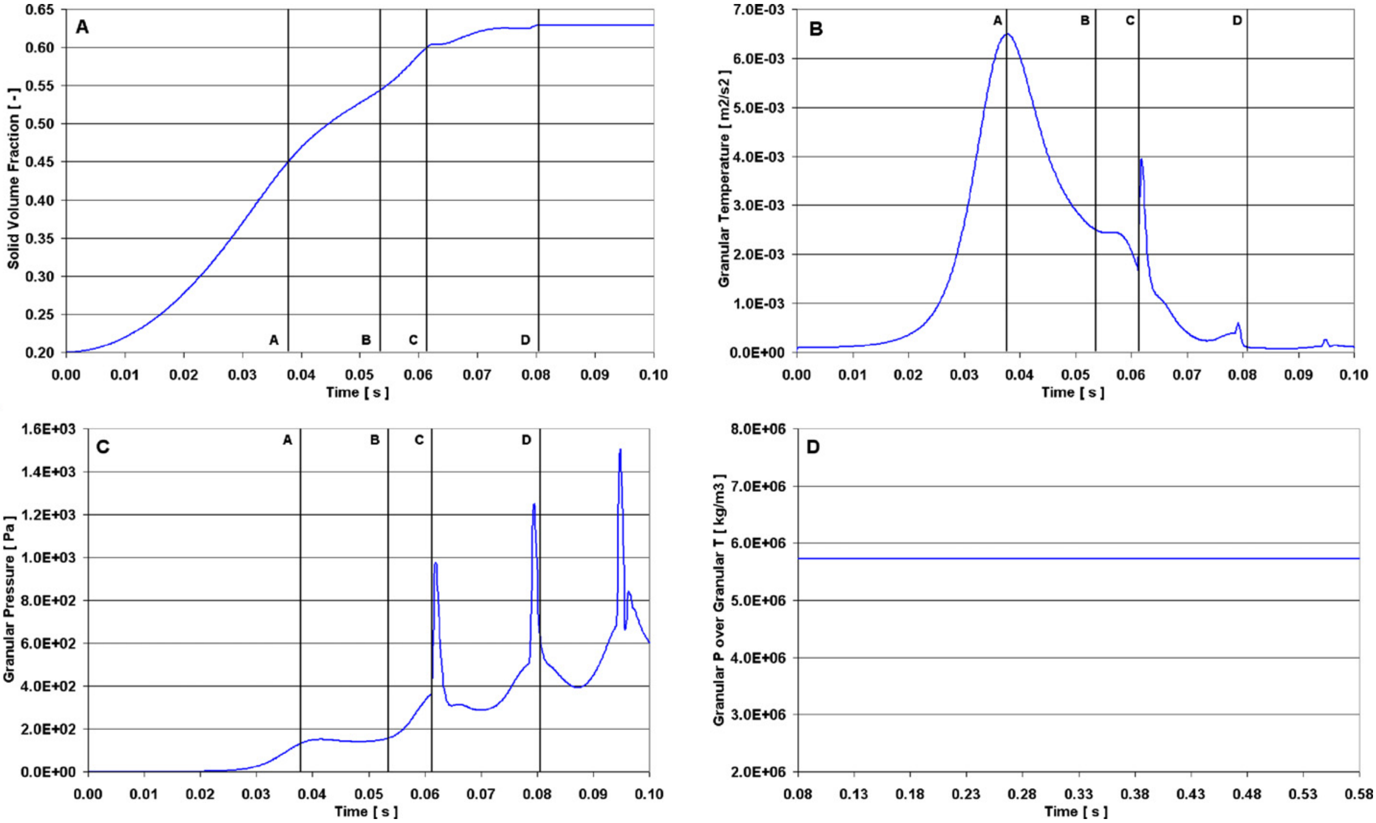

Fig. 3. Solid volume fraction, granular temperature and granular pressure time profiles in the reference location of the bed during the bed collapse. The plastic solid stress is accounted for. The time step is equal to 10^{-4} s.

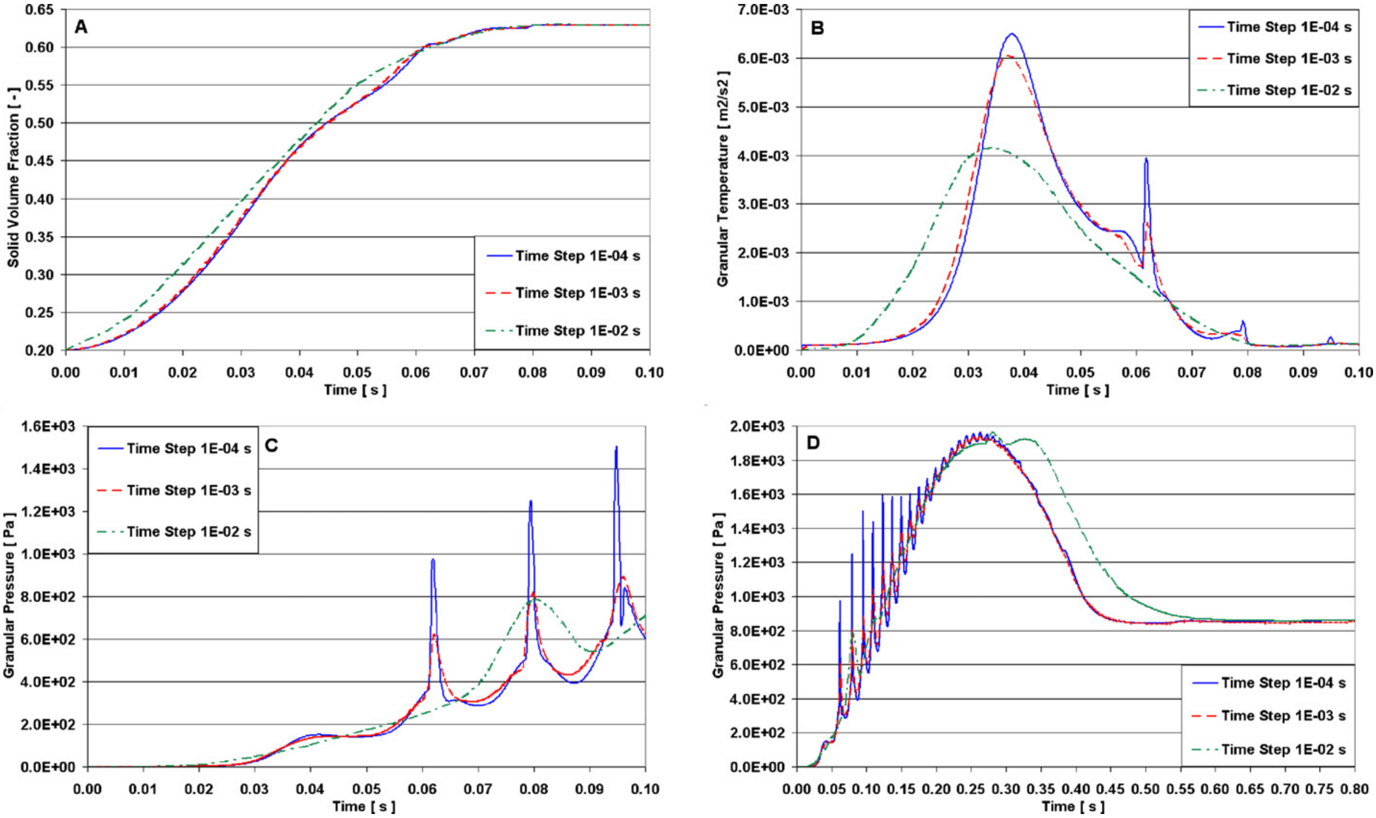

Fig. 4. Solid volume fraction, granular temperature and granular pressure time profiles in the reference location of the bed during the bed collapse. The plastic solid stress is accounted for. The time steps are equal to 10^{-4}, 10^{-3} and 10^{-2} s.

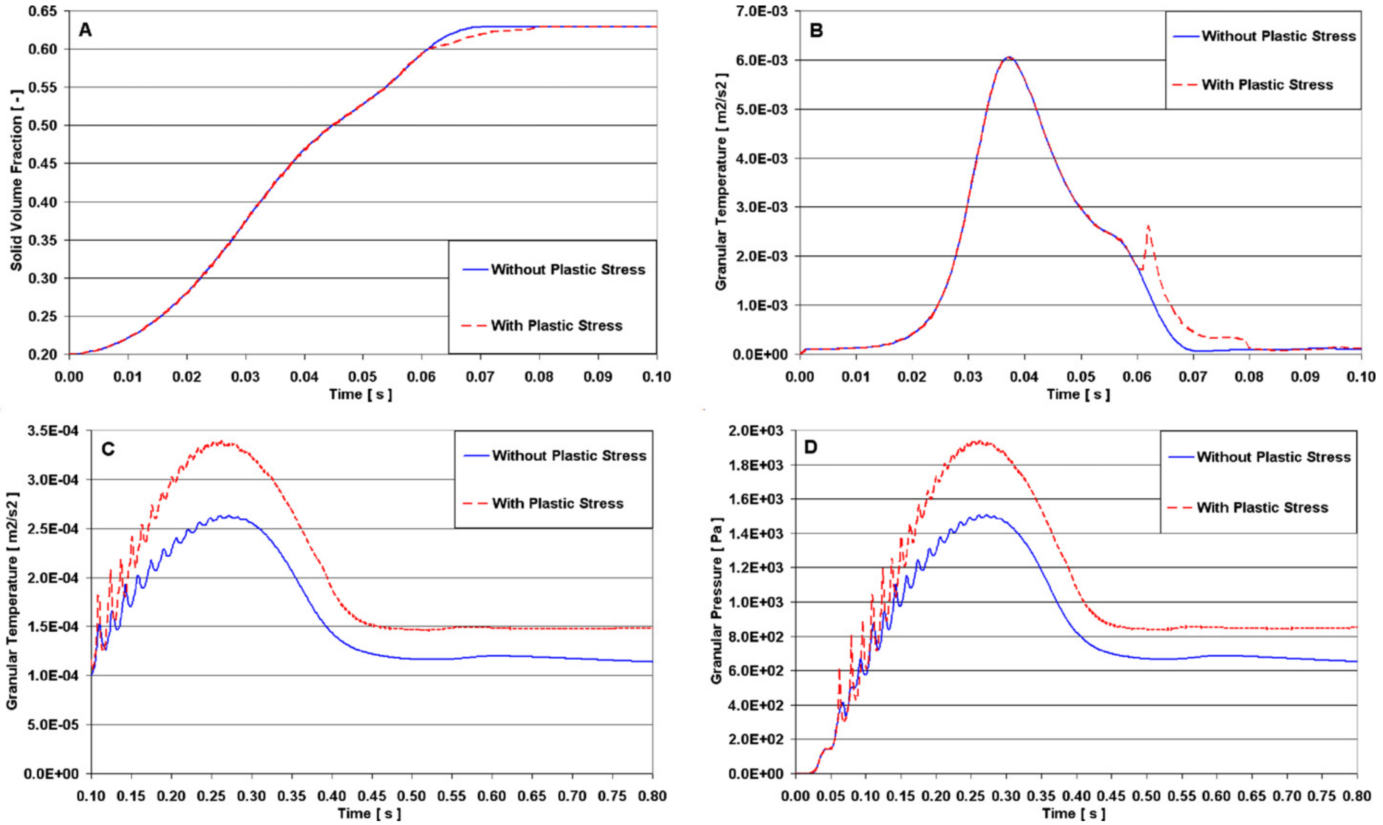

Fig. 5. Solid volume fraction, granular temperature and granular pressure time profiles in the reference location of the bed during the bed collapse. The plastic solid stress is in one case neglected and in one case accounted for. The time step is equal to 10^{-3} s.

merely 0.010 real time seconds, but as we shall presently see it has important consequences.

Fig. 4 reports the same profiles shown in Fig. 3 for the three different time steps used. The results that we obtain when employing a time step of 10^{-2} s differ from those yielded by the other two simulations, which are instead very similar; in particular, the profiles obtained in the first case are much smoother than the others, because the time step is too big to capture all the fluctuations. The stationary values, nevertheless, are identical and are also reached in roughly the same time (we refer here to real time, of course, and not computational time). Note that the simulation that employs the biggest time step now does not crash; this is because the increments in volume fraction, once the frictional threshold is reached, are reduced by the plastic stress and the ensuing higher granular pressure. This, as already pointed out, increases the numerical stability, preventing mass imbalance.

8.3. Comparison and conclusions

This analysis tells us that to obtain accurate results we should use a time step of 10^{-3} s. Smaller time steps yield essentially the same results, whereas bigger can either make the simulation crash, if we neglect the plastic stress, or lead to inaccurate predictions. Only for cursory analyses, we should use a time step of 10^{-2} s, and in this case accounting for the plastic stress is essential.

To complete this investigation, we now compare the results obtained with a time step of 10^{-3} s when considering and neglecting the plastic stress. Fig. 5 reports the profiles of solid volume fraction, granular temperature and granular pressure for both simulations. Fig. 5A highlights that the plastic stress slows down compaction when the suspension becomes dense. Fig. 5B indicates that when the system enters the plastic regime, the plastic viscosity initially leads to higher granular temperatures, but eventually Θ_p drops down to roughly the same value. Fig. 5C shows that the stationary value of Θ_p is slightly higher when we account for the plastic stress; being very small, this difference does not show in Fig. 5B and we need a blow up to highlight it. When ϕ becomes stationary, $p_p(\phi, \Theta_p)$ perfectly mirrors Θ_p; this appears in Fig. 5D, where the stationary value of the solid pressure is slightly higher when we account for the plastic stress, similarly to what we found for Θ_p.

9. CFD simulations of segregating fluidized bidisperse mixtures

Initially the mixture is perfectly mixed with a jetsam volume fraction on a fluid-free basis $\bar{\omega}_1$ equal to 0.50. Marzocchella et

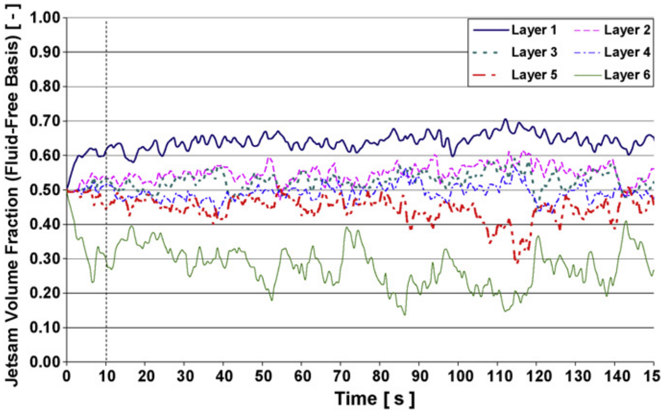

Fig. 6. Time profiles of the average jetsam volume fractions on a fluid-free basis in the six bed layers for a fluid velocity of 5.00 cm/s.

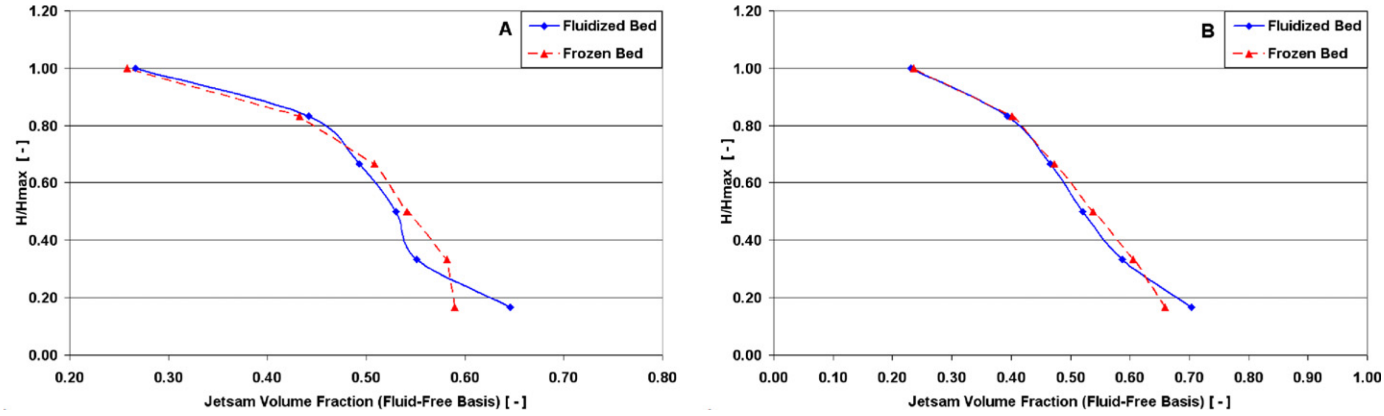

Fig. 7. Stationary axial profiles of the average jetsam volume fractions on a fluid-free basis in the six bed layers obtained before and after freezing the bed for fluid velocities of 5.00 (A) and 7.00 (B) cm/s.

al. [2] experimentally showed that this system starts segregating at a superficial fluid velocity $u_1(\bar{\omega}_1) = 2.00\,\text{cm/s}$ and becomes steadily fluidized and fully mixed at $u_2(\bar{\omega}_1) = 9.00\,\text{cm/s}$. To determine numerically these parameters, we ran a set of simulations at different superficial fluid velocities, finding for each velocity u a stationary profile of jetsam volume fractions (fluid-free basis) along the upward vertical axis x of the bed. To get these profiles, we divided the bed in six horizontal layers of equal height and computed the average values $\langle\omega_1\rangle(x_i)$ of jetsam volume fraction within each layer, assigning them to the heights x_i of the layer upper boundaries. Marzocchella et al. used the same procedure in their experiments, first making the fluidized bed collapse by cutting off the fluid supply (*bed freezing*), then dividing the bed in six layers and finally determining the average jetsam concentrations by sieving the powder collected in each layer. Computationally, freezing the bed is not necessary, since we can easily determine the fluid-free jetsam volume fractions while the mixture is fluidized. To see whether there is any difference, we computed the profiles in both cases, for fluidized and frozen beds.

In each simulation, the system reaches pseudostationary conditions within ten seconds. Fig. 6 reports, as an example, the time profiles of the functions $\langle\omega_1\rangle(x_i, t)$ for a velocity u of 5.00 cm/s. As we can see, after ten seconds the profiles become roughly periodic. Since we observed similar trends also in all the other simulations, we computed the steady-state values always by averaging between $t_A = 10\,\text{s}$ and $t_B = 150\,\text{s}$, which is the last simulated instant; thus, it is:

$$\langle\omega_1\rangle(x_i) \equiv \frac{1}{t_B - t_A}\int_{t_A}^{t_B} \langle\omega_1\rangle(x_i, t)dt \tag{9.1}$$

Fig. 7 shows the average jetsam concentration profiles that we obtained before and after freezing the bed, for fluid velocities equal to 5.00 and 7.00 cm/s (Fig. 7A and B, respectively). Because fluidized and frozen beds have different heights, to compare the results we normalized x_i with respect to the overall bed height, equal to x_6. In the top two layers, *i.e.*, for $i = 5, 6$, $\langle\omega_1\rangle(x_i)$ does not vary significantly; in the three lower layers, *i.e.*, for $i = 2, 3, 4$, it slightly increases, with a maximum percent variation of 5.6%; finally, in the bottom layer it slightly decreases, with a maximum percent variation of 8.6%.

To explain these variations, we must consider the collapsing bed dynamics. In the experiments, the bed freezing is almost instantaneous, especially if the fluid trapped in the bed and in the windbox leaves them partially through a vent valve connected to the latter. Conversely, the simulated collapse is not instantaneous and takes about two seconds to complete, as Fig. 8 indicates. As the mixture collapses, the powder in the bottom layer is partly pushed down-

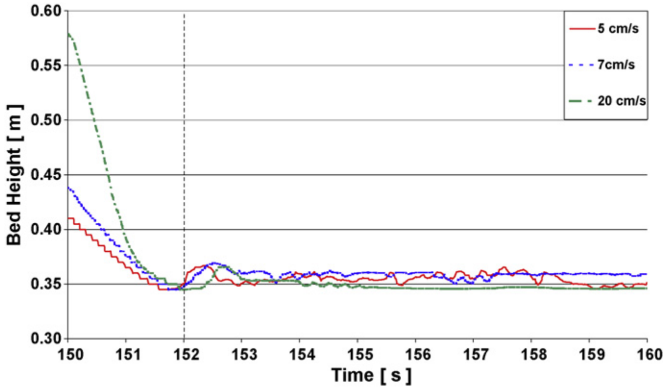

Fig. 8. Bed height time profiles during bed collapses of mixtures initially fluidized at fluid velocities of 5.00, 7.00 and 20.00 cm/s.

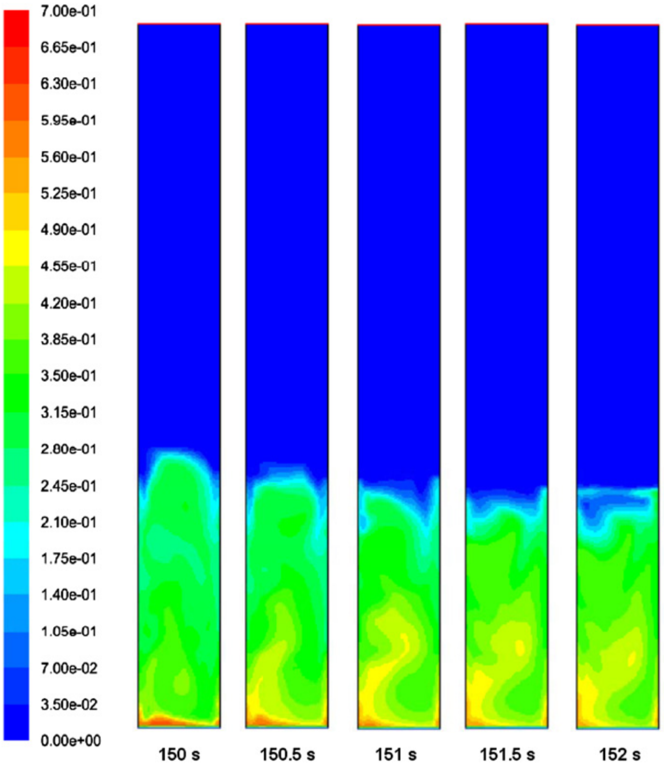

Fig. 9. Time evolution of the jetsam volume fraction spatial profiles during the collapse of the binary mixture initially fluidized at a fluid velocity of 5.00 cm/s.

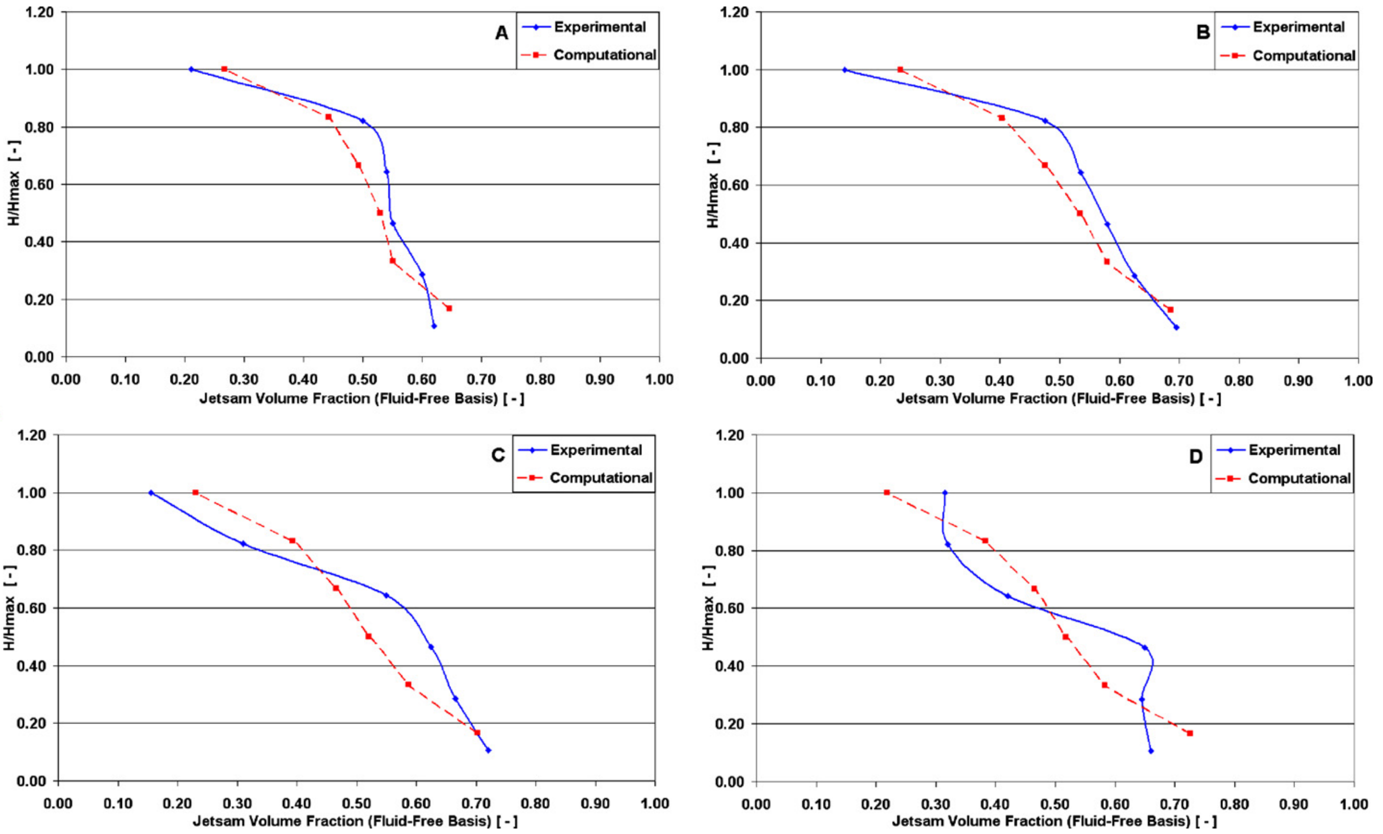

Fig. 10. Stationary axial profiles of the average jetsam volume fractions on a fluid-free basis in the six bed layers for fluid velocities of 5.00 (A), 6.00 (B), 7.00 (C) and 8.00 (D) cm/s. Comparison between computational and experimental values.

wards from the center of the bed towards its periphery and then upwards along the vessel walls. This mechanism induces mixing and alters the segregation profiles. Fig. 9, which refers to a fluid velocity of 5.00 cm/s, shows visually this phenomenon, reporting how the jetsam volume fraction evolves in time and space as the bed collapses.

In light of these considerations, to validate the numerical results we decided to employ the concentration profiles computed while the bed is fluidized. There is, nevertheless, also another reason. At high superficial fluid velocities, near the jetsam minimum fluidization velocity, bubbling is vigorous, and thus the functions $\langle\omega_1\rangle(x_i, t)$ oscillate violently. The bed partially segregates, but then the bubbles remix the mixture, evening out the jetsam axial concentration. In these conditions, it is best to simulate the bed dynamics for a sufficient long time and then average the functions $\langle\omega_1\rangle(x_i, t)$ over many fluctuations. Freezing the bed, conversely, can lead to different profiles $\langle\omega_1\rangle(x_i)$ depending on when we stop feeding the fluid.

Fig. 10 reports the numerical and experimental values of $\langle\omega_1\rangle(x_i)$, the latter obtained by Marzocchella et al., for fluid velocities of 5.00, 6.00, 7.00 and 8.00 cm/s. Qualitatively, the trends are correctly captured; the average percent error in the predictions is of about 11.0%, with the exception of the top layer where it increases to about 40.0%, the segregation being here overpredicted. In both experiments and simulations, the bed does not separate sharply in two uniform layers, but $\langle\omega_1\rangle(x_i)$ changes gradually through the bed.

As we previously mentioned, Marzocchella et al. observed that for fluid velocities less than 2.00 cm/s the powder forms a fixed bed, whereas for velocities greater than 9.00 cm/s it turns into a steadily fluidized, well-mixed suspension. Between these two thresholds, the suspension segregates and is partially defluidized, the defluidized region being nearly at incipient fluidization. To test the simulations on this, we first computed the pressure drop through the bed, $\Delta p(u)$, comparing it with the bed weight per unit cross-sectional area, $\Delta p_e(u)$. For $u \geq 2.00$ cm/s, we found that the two are equal, the fluid entirely supporting the particles; at lower fluid velocities, conversely, $\Delta p(u) < \Delta p_e(u)$. As an example, Fig. 11 reports the pressure drop through the bed against time for fluid velocities of 0.50, 1.00 and 2.00 cm/s. For the first two velocities, $\Delta p(u) < \Delta p_e(u)$, with the distributor plate supporting about 1.0% and 0.5% of the bed weight, respectively; for the third, conversely, $\Delta p(u) \approx \Delta p_e(u)$.

From the pressure drop standpoint, the computational predictions might seem to agree reasonably well with the experimental evidence. But can we claim to have correctly predicted $u_1(\bar{\omega}_1)$?

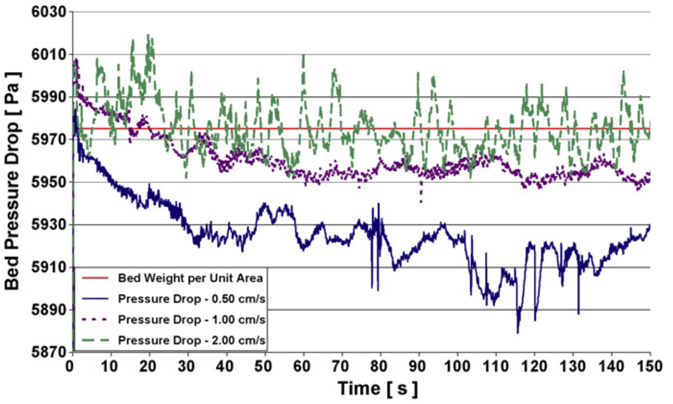

Fig. 11. Bed pressure drop time profiles for fluid velocities of 0.50, 1.00 and 2.00 cm/s.

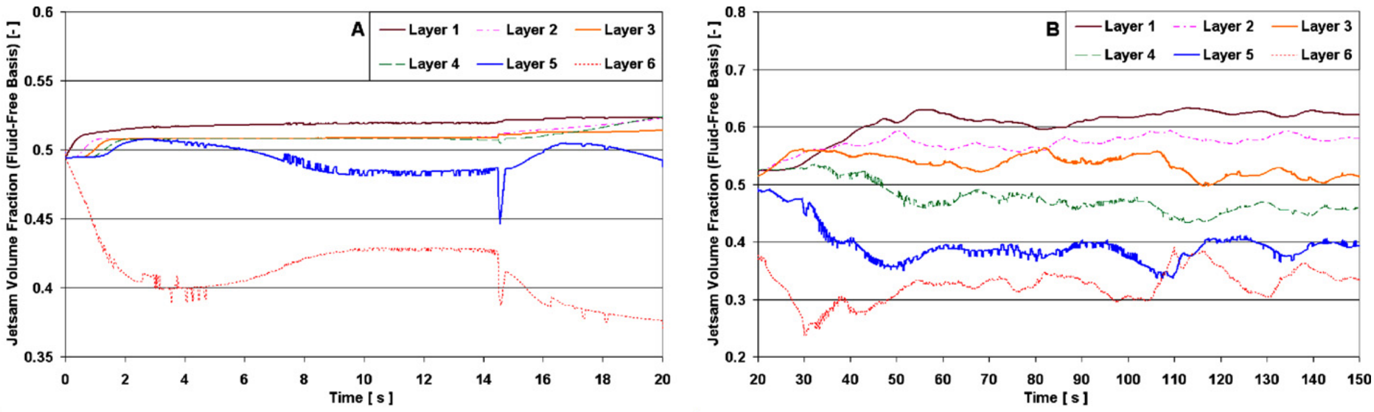

Fig. 12. Time profiles of the average jetsam volume fractions on a fluid-free basis in the six bed layers for a fluid velocity of 1.00 cm/s.

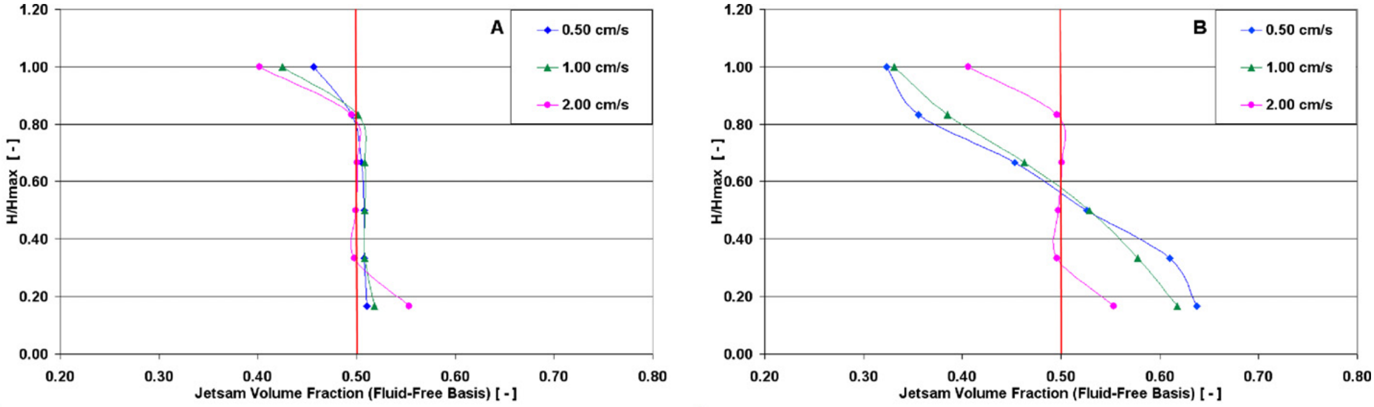

Fig. 13. Stationary axial profiles of the average jetsam volume fractions on a fluid-free basis in the six bed layers for fluid velocities of 0.50, 1.00 and 2.00 cm/s. (A) reports values averaged between 10 and 20 s; (B) reports values averaged between 60 and 150 s.

For $u < 2.00\,\mathrm{cm/s}$, we know that $\Delta p(u) < \Delta p_e(u)$ and that the gas distributor plate supports part of the bed weight. What we still do not know is whether the bed is fixed or partially fluidized. In the first case, transient fluidization does not take place, the mixture does not segregate and $\langle\omega_1\rangle(x_i) = \bar{\omega}_1$ for any x_i; then it must be $u_1(\bar{\omega}_1) \approx 2.00\,\mathrm{cm/s}$. In the second case, the mixture segregates, giving rise to an axial profile in $\langle\omega_1\rangle(x_i)$; consequently, it must be $u_1(\bar{\omega}_1) < 2.00\,\mathrm{cm/s}$. Hence, to understand if the simulations predict correctly $u_1(\bar{\omega}_1)$, we need to examine the segregation profiles for fluid velocities less than 2.00 cm/s. We performed this analysis, finding that the system responds differently depending on the time interval considered. Fig. 12, which refers to a velocity of 1.00 cm/s, reports the average jetsam concentrations $\langle\omega_1\rangle(x_i, t)$ in the six bed layers as time advances. As usual, within the first ten seconds the system attains a pseudostationary state (Fig. 12A). But after 20 s, a new dynamics arises, and the functions $\langle\omega_1\rangle(x_i, t)$ start changing again towards new equilibrium values (Fig. 12B), with the mixture much more segregated.

Let us first consider the time interval between 0 s and 20 s. Fig. 13A reports the jetsam concentrations $\langle\omega_1\rangle(x_i)$ averaged between 10 s and 20 s. For $u < 2.00\,\mathrm{cm/s}$, the bed is nearly fixed, with $\langle\omega_1\rangle(x_i) \approx \bar{\omega}_1$ for any x_i except in the top layer where the jetsam slightly segregates. For $u = 2.00$ cm/s, $\langle\omega_1\rangle(x_i)$ changes in both top and bottom layers, remaining roughly constant in the four middle layers. This analysis suggests that, at least for the fluid velocities considered, the powder is never perfectly fixed, but some dynamics is always present. Thus, strictly speaking, $u_1(\bar{\omega}_1)$ must be lower than 0.50 cm/s. However, if we neglect what happens in the top bed layer, we might assume $u_1(\bar{\omega}_1) \approx 2.00\,\mathrm{cm/s}$, because for higher fluid velocities bed dynamics and segregation are more pronounced.

After 20 s, a mixture that up to that moment had been fixed begins to segregate. Fig. 13B reports the values of $\langle\omega_1\rangle(x_i, t)$ averaged between 60 s and 150 s; for $u < 2.00\,\mathrm{cm/s}$ the profiles change, remaining instead the same for $u = 2.00\,\mathrm{cm/s}$. This behavior, where the model predicts segregation even at low fluid velocities, when segregation should not occur, arises in packed beds and was also observed by [46]. It reveals a shortcoming of the interparticle drag

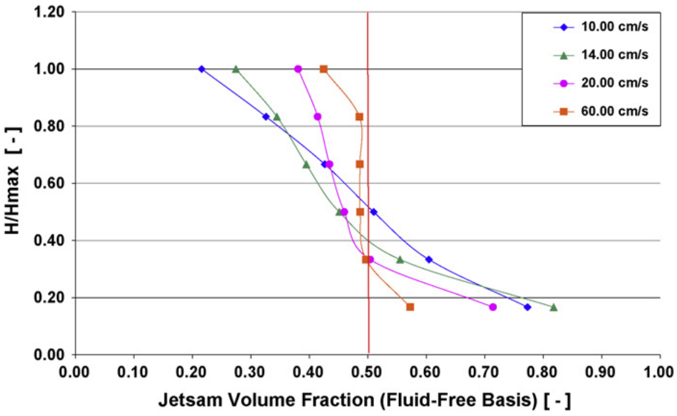

Fig. 14. Stationary axial profiles of the average jetsam volume fractions on a fluid-free basis in the six bed layers for fluid velocities of 10.00, 14.00, 20.00 and 60.00 cm/s.

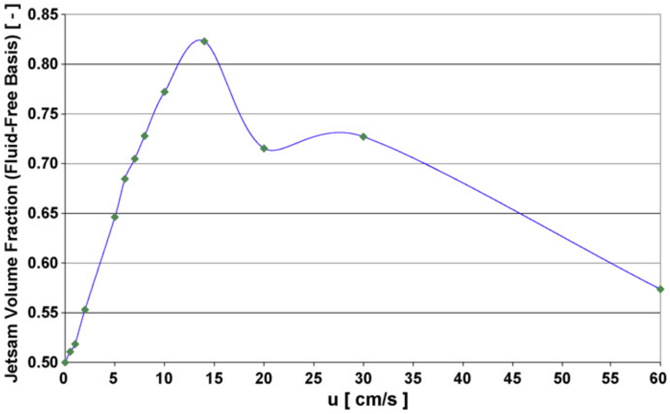

Fig. 15. Stationary values of the average jetsam volume fractions on a fluid-free basis in the bottom bed layer for different fluid velocities.

force closure, which does not diverge when the bed packs up; this prevents the slip velocities between the solid phases from vanishing, allowing segregation to take place. The values $\langle\omega_1\rangle(x_i)$ not changing for $u = 2.00$ cm/s corroborate the idea that this velocity is enough to fluidize the mixture and well approximates $u_1(\bar{\omega}_1)$.

For fluid velocities $u > 9.00$ cm/s, Marzocchella et al. tell us that the mixture is steadily fluidized and fully mixed; they do not report any concentration profiles, so we have to assume that $\langle\omega_1\rangle(x_i) \approx \bar{\omega}_1$ for any x_i. This condition is numerically observed only for fluid velocities much greater than the jetsam minimum fluidization velocity. Fig. 14 reports the values of $\langle\omega_1\rangle(x_i)$, averaged between 10 s and 150 s, for various velocities greater than 9.00 cm/s; even at 60.00 cm/s, which is roughly three times the jetsam minimum fluidization velocity, $\langle\omega_1\rangle(x_i) \neq \bar{\omega}_1$ in the top and bottom bed layers (that is, for $i = 1, 6$). Fig. 15 reports the average jetsam concentration $\langle\omega_1\rangle(x_1)$ in the bottom bed layer (that is, where jetsam segregation should be maximum) as a function of the fluid velocity u. At 60.00 cm/s $\langle\omega_1\rangle(x_1)$ is still greater than $\bar{\omega}_1$; hence, even if qualitatively the trends are correct, the model does not predict well $u_2(\bar{\omega}_1)$.

10. Conclusions

This work tests a basic multifluid model implemented within the commercial computational fluid dynamics code Fluent 6.3; it comprises some preliminary simulations of collapsing monodisperse beds that focuses on the plastic stress role and on the selection of the numerical time step, and an investigation of segregating fluidized binary mixtures. From these analyses, we concluded that:

(1) Radial distribution functions that diverge in ϕ_{max} handle correctly the transition of fluidized suspensions from compressible to incompressible flow regimes. When the solid tends to overpack, g_i and in turn the viscous solid pressure diverge, pushing the particles towards less dense regions of the bed and preventing the powder from reaching unphysically high concentrations. The plastic stress, nevertheless, is important because, by slowing down the packing dynamics, renders the simulations more stable, allowing in some cases for larger time steps. With divergent radial distribution functions, we can neglect the plastic solid pressure, but we should account for the plastic solid viscosity. By increasing the irreversible conversion of mechanical energy into pseudointernal energy, this increases the granular temperature and in turn the viscous solid pressure, slowing down solid packing.

(2) Segregating fluidized bidisperse suspensions are characterized by two velocities, which we denoted by $u_1(\bar{\omega}_1)$ and $u_2(\bar{\omega}_1)$. The first is the minimum velocity at which the bed is no longer fixed, the particles start moving, transient fluidization occurs and the bed pressure drop begins oscillating, while the second is the minimum velocity necessary to steadily fluidize and fully mix the suspension. $u_1(\bar{\omega}_1)$ and $u_2(\bar{\omega}_1)$ depend on the powder composition, but if the particles only differ in size, they usually lie between the minimum fluidization velocities of flotsam and jetsam. The multifluid model employed, to which Fluent refers as KTGF-based model, yields correct qualitative trends and predicts reasonably well the stationary axial profiles of jetsam concentration for fluid velocities between $u_1(\bar{\omega}_1)$ and $u_2(\bar{\omega}_1)$.

(3) For velocities less then $u_1(\bar{\omega}_1)$, the simulated bed is initially fixed, its composition not changing, except in the top layer where some jetsam segregates; also, the pressure drop through the bed is less than the solid weight per unit cross-sectional area. At higher velocities, the mixture is more mobile, segregation is more pronounced and the bed pressure drop balances the solid weight. Therefore, the model seems to estimate well $u_1(\bar{\omega}_1)$. Nevertheless, for $u < u_1(\bar{\omega}_1)$, if we let sufficient time pass, the powder begins to segregate, even if the bed is packed, and the system evolves towards a new steady state. This behavior, also observed by [46], takes place in packed beds and reveals a limitation of the interparticle drag force closure. When the bed is fixed, this force should diverge, making the slip velocities between the solid phases vanish, so that they cannot segregate. This does not happen, and accordingly the powder segregates even when it is fully packed.

(4) The model fails to predict $u_2(\bar{\omega}_1)$, overestimating its value. To prevent segregation, especially in the top and bottom bed layers, the fluid velocity needs to exceed the jetsam minimum fluidization velocity. This might be because the simulated bubble dynamics is less vigorous than the one observed experimentally, and therefore the turbulent motion that establishes at high fluid velocities becomes essential for a powder to become well mixed.

(5) Finally, we found that to determine the stationary jetsam concentration profile along the bed, we should avoid freezing the bed. This is for two reasons. First, the bed takes time to settle down, and as it does so the dynamics alters the original concentration profiles. Second, because at high fluid velocities bubbling makes the jetsam concentration fluctuate, freezing the bed can lead to different profiles, which depend on the bed configuration present when we stop feeding fluid.

References

[1] L. Mazzei, P. Lettieri, A drag force closure for uniformly-dispersed fluidized suspensions, Chem. Eng. Sci. 62 (2007) 6129.
[2] A. Marzocchella, P. Salatino, V. Di Pastena, L. Lirer, Transient fluidization and segregation of binary mixtures of particles, AIChE J. 46 (2000) 2175.
[3] P.N. Rowe, A.W. Nienow, Particle mixing and segregation in gas fluidized beds—a review, Powder Technol. 15 (1976) 141.
[4] P.N. Rowe, A.W. Nienow, Minimum fluidisation velocity of multicomponent particle mixtures, Chem. Eng. Sci. 30 (1975) 1365.
[5] K. Noda, S. Uchida, T. Makino, H. Kamo, Minimum fluidisation velocity of binary mixture of particles with large size ratio, Powder Technol. 46 (1986) 149.
[6] B. Formisani, Packing and fluidisation properties of binary mixtures of spherical particles, Powder Technol. 66 (1991) 259.
[7] B. Formisani, G. De Cristoforo, R. Giramonte, A fundamental approach to the phenomenology of fluidisation of size segregating binary mixtures of solids, Chem. Eng. Sci. 56 (2001) 109.
[8] K. Yoshida, H. Kameyama, F. Shimizu, Mechanism of particle mixing and segregation in gas fluidized beds, in: J.R. Grace, J.M. Matsen (Eds.), Fluidization, Plenum, 1980.
[9] B. Kozanoglu, E.K. Levy, Mixing dynamics in bubbling fluidized bed with binary solids, in: O.E. Potter, D.J. Nicklin (Eds.), Fluidization VII, Engineering Foundation, 1992.
[10] G. Olivieri, A. Marzocchella, P. Salatino, Segregation of fluidized binary mixtures of granular solids, AIChE J. 50 (2004) 3095.

[11] G. Olivieri, A. Marzocchella, P. Salatino, A fluid-bed continuous classifier of polydisperse granular solids, in: Proc. of the 2006 AIChE Spring National Meeting, Orlando, USA, 2006.

[12] L.G. Gibilaro, P.N. Rowe, A model for a segregating gas fluidized bed, Chem. Eng. Sci. 29 (1974) 1403.

[13] N.S. Naimer, T. Chiba, W.A. Nienow, Parameter estimation for a solids mixing/segregation model for a gas fluidised bed, Chem. Eng. Sci. 37 (1982) 1047.

[14] P.J.M. Valkenburg, J.C. Schouten, C.M. van den Bleek, The non-steady state segregation of particles in gas fluidized beds, in: K. Ostregaard, A. Sorensen (Eds.), Fluidization V, United Engineering Trustees, 1986.

[15] W.C. Yang, D.L. Keairns, Further studies on the rate of particle separation in gas-fluidized bed, J. Chin. Inst. Chem. Eng. 22 (1991) 419.

[16] J.Y. Kim, K.Y. Choi, Polymer particle mixing and segregation in a gas phase olefin polymerization reactor, in: AIChE Symposium Series, vol. 95, 1999, p. 77.

[17] B.P.B. Hoomans, J.A.M. Kuipers, W.J. Briels, W.P.M. van Swaaij, Discrete particle simulation of segregation phenomena in dense gas-fluidized beds, in: L.S. Fan, T. Knowlton (Eds.), Fluidization IX, Engineering Foundation, 1998.

[18] Y.Q. Feng, B.H. Xu, S.J. Zhang, A.B. Yu, Discrete particle simulation of gas fluidization of particle mixtures, AIChE J. 50 (2004) 1713.

[19] M. Chiesa, V. Mathiesen, J.A. Melheim, B. Halvorsen, Numerical simulation of particulate flow by the Eulerian–Lagrangian and the Eulerian–Eulerian approach with application to a fluidized bed, Comput. Chem. Eng. 29 (2005) 291.

[20] L. Huilin, Z. Yunhua, J. Ding, D. Gidaspow, L. Wei, Investigation of mixing/segregation of mixture particles in gas-solid fluidized beds, Chem. Eng. Sci. 62 (2007) 301.

[21] T.B. Anderson, R. Jackson, A fluid mechanical description of fluidized beds. Equations of motion, Ind. Eng. Chem. Fundam. 6 (1967) 527.

[22] P. Lettieri, L. Mazzei, Challenges and issues on the CFD modeling of fluidized beds: a review, J. Comput. Multiphase Flows 1 (2009) 83.

[23] S.B. Savage, D.J. Jeffrey, The stress tensor in a granular flow at high shear rates, J. Fluid Mech. 110 (1981) 255.

[24] J.T. Jenkins, S.B. Savage, A theory for the rapid flow of identical, smooth, nearly elastic, spherical particles, J. Fluid Mech. 130 (1983) 187.

[25] D. Gidaspow, Multiphase Flow and Fluidization, Academic Press, 1994.

[26] J.T. Jenkins, F. Mancini, Kinetic theory for binary mixtures of smooth, nearly elastic spheres, Phys. Fluids 31 (1989) 2050.

[27] M. Syamlal, The particle-particle drag term in a multiparticle model of fluidization, National Technical Information Service, DOE/MC/21353–2373, NTIS/DE87006500, 1987.

[28] P. Zamankhan, Kinetic theory of multicomponent dense mixtures of slightly inelastic spherical particles, Phys. Rev. 52 (1995) 4877.

[29] D. Gidaspow, L. Huilin, E. Mangar, Kinetic theory of multiphase flow and fluidization: validation and extension to binaries, in: Proc. of the 19th International Congress on Theoretical and Applied Mechanics, Kyoto, Japan, 1996.

[30] L. Huilin, H. Yurong, D. Gidaspow, Y. Lidan, Q. Yukun, Size segregation of binary mixture of solids in bubbling fluidized beds, Powder Technol. 134 (2003) 86.

[31] B.G.M. van Wachem, J.C. Schouten, C.M. van den Bleek, R. Krishna, J.L. Sinclair, CFD modeling of gas-fluidized beds with a bimodal particle mixture, AIChE J. 47 (2001) 1292.

[32] S. Cooper, C.J. Coronella, CFD simulations of particle mixing in a binary fluidized bed, Powder Technol. 151 (2005) 27.

[33] L. Mazzei, Eulerian modelling and computational fluid dynamics simulation of mono and polydisperse fluidized suspensions, Ph.D. Dissertation, Department of Chemical Engineering, University College London, 2008.

[34] M.R. Maxey, J.J. Riley, Equation of motion for a small rigid sphere in a nonuniform flow, Phys. Fluids 26 (1983) 883.

[35] O. Owoyemi, L. Mazzei, P. Lettieri, CFD modeling of binary-fluidized suspensions and investigation of role of particle-particle drag on mixing and segregation, AIChE J. 53 (2007) 1924.

[36] J.M. Dallavalle, Micromeritics, Pitman, 1948.

[37] J.F. Richardson, W.N. Zaki, Sedimentation and fluidization: Part I, Trans. Inst. Chem. Eng. 32 (1954) 35.

[38] P.N. Rowe, A convenient empirical equation for estimation of the Richardson and Zaki exponent, Chem. Eng. Sci. 42 (1987) 2795.

[39] R.F. Fedors, R.F. Landel, An empirical method of estimating the void fraction in mixtures of uniform particles of different size, Powder Technol. 23 (1979) 225.

[40] R. Jackson, The Dynamics of Fluidized Particles. Cambridge Monographs on Mechanics, Cambridge University Press, 2000.

[41] C.K.K. Lun, S.B. Savage, D.J. Jeffrey, N. Chepurniy, Kinetic theories for granular flow: inelastic particles in Couette flow and slightly inelastic particles in a general flow field, J. Fluid Mech. 140 (1984) 223.

[42] M. Syamlal, W.A. Rogers, T.J. O'Brien, MFIX Documentation and Theory Guide, DOE/METC94/1004, NTIS/DE94000087, Electronically available from: http://www.mfix.org, 1993.

[43] D.G. Schaeffer, Instability in the evolution equations describing incompressible granular flow, J. Differ. Eq. 66 (1987) 19.

[44] D.G. Schaeffer, E.B. Pitman, Ill-posedness in three-dimensional plastic flow, Commun. Pure Appl. Math. 41 (1988) 879.

[45] S.M. Lo, Mathematical basis of a multiphase flow model, AERE R 13432, 1989.

[46] D. Gera, M. Syamlal, T.J. O'Brien, Hydrodynamics of particle segregation in fluidized beds, Int. J. Multiphase Flow 30 (2004) 419.